Geochemistry, Geophysics, Geosystems

RESEARCH ARTICLE
10.1029/2020GC008922

Key Points:
- We characterize the chemical weathering of loess deposits
- The glacial-interglacial variability of global chemical weathering fluxes is analysed

Supporting Information:
- Supporting Information S1

Correspondence to:
J. Börker and J. Hartmann,
janine.boerker@uni-hamburg.de;
geo@hattes.de

Citation:
Börker, J., Hartmann, J., Amann, T., Romero-Mujalli, G., Moosdorf, N., & Jenkins, C. (2020). Chemical weathering of loess and its contribution to global alkalinity fluxes to the coastal zone during the Last Glacial Maximum, Mid-Holocene, and Present. *Geochemistry, Geophysics, Geosystems*, *21*, e2020GC008922. https://doi.org/10.1029/2020GC008922

Received 13 JAN 2020
Accepted 1 APR 2020
Accepted article online 30 MAY 2020

Chemical Weathering of Loess and Its Contribution to Global Alkalinity Fluxes to the Coastal Zone During the Last Glacial Maximum, Mid-Holocene, and Present

Janine Börker[1], Jens Hartmann[1], Thorben Amann[1], Gibran Romero-Mujalli[1,2], Nils Moosdorf[3,4], and Chris Jenkins[5]

[1]Institute for Geology, CEN (Center for Earth System Research and Sustainability), Universität Hamburg, Hamburg, Germany, [2]Instituto de Ciencias de la Tierra (ICT), Facultad de Ciencias, Universidad Central de Venezuela (UCV), Caracas, Venezuela, [3]Leibniz Centre for Tropical Marine Research (ZMT), Bremen, Germany, [4]Institute of Geosciences, University of Kiel, Kiel, Germany, [5]Institute of Arctic and Alpine Research, University of Colorado Boulder, Boulder, CO, USA

Abstract Loess sediments are windblown silt deposits with, in general, a carbonate grain content of up to 30%. While regionally, loess was reported to increase weathering fluxes substantially, the influence on global weathering fluxes remains unknown. Especially on glacial-interglacial time scales, loess weathering fluxes might have contributed to land-ocean alkalinity flux variability since the loess areal extent during glacial epochs was larger. To quantify loess weathering fluxes, global maps representing the loess distribution were compiled. Water chemistry of rivers draining recent loess deposits suggests that loess contributes over-proportionally to alkalinity concentrations if compared to the mean of alkalinity concentrations of global rivers (~4,110 μeq L^{-1} for rivers draining loess deposits and ~1,850 μeq L^{-1} for the total of global rivers), showing comparable alkalinity concentration patterns in rivers as found for carbonate sedimentary rocks. Loess deposits, covering ~4% of the ice- and water-free land area, increase calculated global alkalinity fluxes to the coastal zone by 16%. The new calculations lead to estimating a 4% higher global alkalinity flux during the Last Glacial Maximum (LGM) compared to present fluxes. The effect of loess on that comparison is high. Alkalinity fluxes from silicate-dominated lithological classes were ~28% and ~30% lower during the LGM than recent (with loess and without loess, respectively), and elevated alkalinity fluxes from loess deposits compensated for this. Enhanced loess weathering dampens due to a legacy effect changes in silicate-dominated lithologies over the glacial-interglacial time scale.

1. Introduction

Loess sediments cover extensive areas on the Earth's surface (Muhs et al., 2014). They can provide insights into dynamical sedimentation processes of the past and serve as terrestrial archives for studying dust deposition and atmospheric circulation (Muhs & Bettis, 2000; Muhs et al., 2014; Schaetzl et al., 2018). While loess sediments are widespread around the globe, they are mainly abundant in middle latitudes. Nowadays, they cover about 4.9×10^6 km^2 (Börker et al., 2018), which represents about 4% of the total ice-free land area (i.e., relative to the Global Lithological Map [GLiM] area without ice and water bodies; Hartmann & Moosdorf, 2012).

In this study, loess deposits are defined as windblown silt deposits which typically contain quartz, feldspar, mica, and clay minerals, but also carbonate minerals (Muhs et al., 2014; Pye, 1984; Smalley et al., 2011). Besides their significance to climate-related studies, loess sediments are assumed to be important regarding chemical weathering fluxes, and their weathering behavior, including, for example, weathering proxies, has to be understood (e.g., Buggle et al., 2011). Because surfaces of loess sediments are often only slightly weathered, and because of their carbonate content and high surface area due to fine grainsize, loess might have a high influence on global weathering fluxes. Kump and Alley (1994) mention the possible significance of loess deposits in glacial chemical weathering studies. Goddéris et al. (2013) applied numerical models to quantify the weathering of the Mississippi Valley loess to simulate climate, the continental biosphere, and the weathering processes within the pedon. They calculated similar CO_2 consumption rates from

Mississippi Valley loess than those from carbonate sedimentary rocks globally, because of dolomite dissolution being the major contributor to CO_2 consumption, which underlines the possible importance of loess weathering. Zhang et al. (2013) concluded that even in slightly loess-covered areas (18% loess coverage in a lake catchment on the northeastern Chinese Loess Plateau), the weathering processes of loess dominate the weathering fluxes.

Since loess sediments can have a generally high content of carbonate minerals (up to 30% carbonate grains after Pye, 1984), it has to be tested whether they show in general a similar weathering behavior as carbonate rocks. Therefore, alkalinity fluxes from loess areas were studied by analyzing river chemistry data of catchments dominated by loess deposits and compared with alkalinity fluxes derived by applying previous carbonate weathering models (Amiotte-Suchet & Probst, 1995; Bluth & Kump, 1994; Romero-Mujalli, Hartmann, & Börker, 2018). The quantification of riverine alkalinity inputs to the ocean is relevant, since it directly influences marine biogeochemical cycles. Moreover, alkalinity fluxes provide insight into the amount of atmospheric CO_2 that is being consumed by chemical weathering of rocks.

To quantify global changes of alkalinity flux and CO_2 consumption rates, comparing the time of the Last Glacial Maximum (LGM), the Mid-Holocene, and the recent setting, a spatial reconstruction of loess deposits is needed. For this purpose, a map of loess distribution during the LGM was created by extrapolating geographically the recent loess distribution (Börker et al., 2018). This extrapolation includes, for example, alluvial areas which accumulate material from catchment loess deposits during the LGM. For the LGM loess map, present-day inundated continental shelf areas were also considered, since the sea level was ~134 m lower during the LGM (Lambeck et al., 2014), leading to the exposition of large shelf areas to terrestrial weathering. Information about loess sediments on previously exposed continental shelves is included in the LGM loess map in this study.

In the presented study, global alkalinity fluxes and according CO_2 consumption rates by weathering were calculated and compared for the LGM, the Mid-Holocene, and the present day. The comparison of loess weathering areas with carbonate and silicate rock areas was used to address the question if loess has a relevant influence on global alkalinity weathering fluxes for the chosen time slices, considering changes in global climate on hydrology and temperature.

2. Methods

2.1. Current Loess Distribution

The current time loess distribution was obtained from the Global Unconsolidated Sediments Map database (GUM) (Börker et al., 2018). The map distinguishes between subclasses of primary loess deposits, loess derivates, and loess-like silt deposits. In the further analysis, we do not distinguish between the different subtypes of loess. Most of the loess deposits can be found in the middle latitudes, 35–70°N and 25–40°S, respectively (Börker et al., 2018). For the Mid-Holocene scenario, we assume that the loess distribution is similar to the recent one.

2.2. Loess Distribution at the LGM

For the LGM, the land area that is equal to the recent continents had to be increased by the exposed continental shelves due to a lower sea level.

2.2.1. Loess Distribution of the LGM on Continents

Due to a lack of map data, the global loess distribution for the LGM cannot be reconstructed based on ground mapping but can be estimated. Mahowald et al. (1999) state that eolian deposition rates were up to 2–20 times higher during glacial periods, and Rousseau et al. (2014) conclude that the dust deposition fluxes during the LGM might have been 2–3 times higher. Since the Chinese Loess Plateau was reported to be extended to the south of the Yangtze River (25–30°N) (Pinxian & Xiangjun, 1994, and references therein) and river valleys were reported to have once been covered with loess deposits in some regions, before they were eroded (United States Army Corps of Engineers, 1974), the recent loess extent (Börker et al., 2018) had to be larger during the LGM period. As a conservative approach, reconstruction of past loess areas was done using *Esri* ArcMap (v10.6) by extrapolating the recent time loess shapefile, using the Euclidean Distance Tool with a maximum distance of 10 km. By doing this, river valleys within loess deposits, for example, were filled with loess. The constant extrapolation distance might cause additional regional biases because a constant

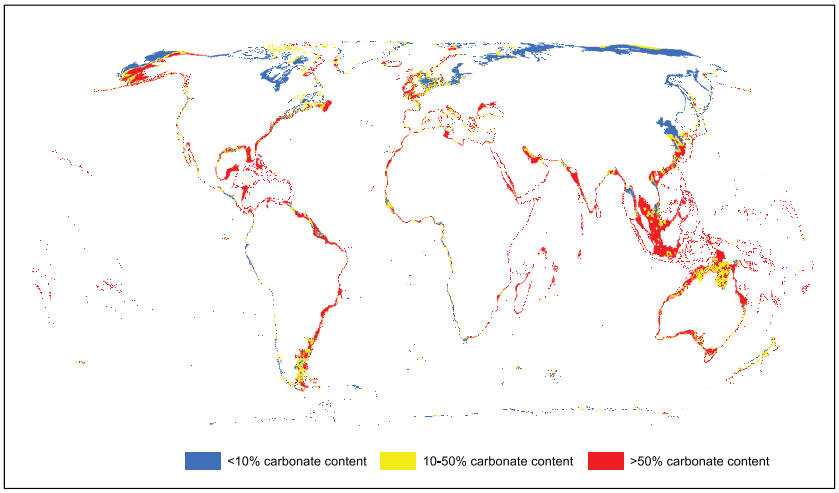

Figure 1. Interpolated carbonate content (resolution: 0.25° × 0.25°) of the modern marine sediments for continental shelves, which were exposed during the LGM, derived by the *dbSEABED* database (Bostock et al., 2018; Goff et al., 2008; Jenkins, 1997, 2018).

Holocene erosion for all global loess regions is assumed and different depositional environments are neglected. The sensitivity of the loess extrapolation method was tested for different scenarios and is additionally discussed in section 3.4.1.

2.2.2. Loess Distribution on Exposed Continental Shelves

To analyze weathering on exposed continental shelves during the LGM, the subaerial shelf extent was determined using the global relief model ETOPO1 (Amante & Eakins, 2009). By setting the bathymetric line to −130 m (a rounded value derived from Lambeck et al., 2014), an exposed continental shelf area of about 23×10^6 km^2 was calculated. After subtracting the area that was covered by ice sheets (Ehlers et al., 2011), the total area of exposed shelves that were affected by weathering is therefore 19×10^6 km^2.

For several regions of the continental shelves, it was possible to reconstruct loess deposits from literature studies and digitize these areas with *GIS*. In the English Channel, evidence for loess deposits was described by Lefort et al. (2013). Extensive loess deposits on the Arctic shelf were made available by Biryukov et al. (1988). For most of the Black Sea, data of shelf loess deposits were made available in Ryan et al. (1997) and for the Argentinian continental shelf by Violante et al. (2014). Besides, data about loess deposits in the China Sea, on the shelves off West Africa, and in the Indian Ocean and Western Pacific (Figure 3) were made available by Li et al. (2013) and references therein. Details on the compilation of loess data of the continental shelves can be found in the supporting information.

2.3. Carbonate Content of the Shelves' Sediments

To quantify alkalinity fluxes from the total continental shelves, which were exposed during the LGM, additional sediment types besides loess were considered. Reconstruction of the sedimentary pattern that was exposed during the LGM is challenging due to strong erosion of the subsequent transgressional phases. As a first assumption, the modern sediments might represent the sediments that were accumulated in the previous sea-level high-stand interglacial period. A global database of chemical, physical, and mineralogical data about the ocean sediments from surface samplings and shallow stratigraphy-penetrating cores was used (*dbSEABED*, Bostock et al., 2018; Goff et al., 2008; Jenkins, 1997, 2018). The database includes the world distribution of coral reefs, which are mostly growing on old karstic low sea-level landscapes (Purdy, 1974), also composed of carbonate. The point data of the carbonate content of all the sediments were interpolated to all shelf areas at a resolution of 0.25° × 0.25° (Figure 1).

For global calculations of alkalinity fluxes, the shelf sediments are reclassified by their carbonate content, based on the carbonate proportions of "hydro"-oriented lithological classes defined in Dürr et al. (2005):

1. non-carbonatic sediments (ss) with in general <10% carbonate content;
2. mixed sediments (sm) with 10% to 50% carbonate content; and

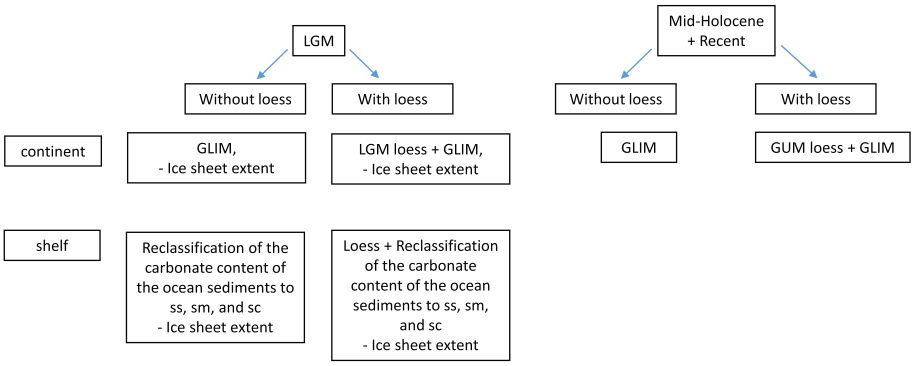

Figure 2. Flowchart of the development of the lithological input data sets for the global calculations. For the Mid-Holocene and the recent time period the same lithological map was used. Loess was, where considered, always preferred over other lithological classes.

3. carbonatic sediments (sc) with >50% carbonate content.

2.4. Hydrochemical Database

To analyze alkalinity fluxes from loess deposits, the Global River Chemistry Database (GLORICH) was used (Hartmann, Lauerwald, et al., 2014; Hartmann et al., 2019). This database comprises 1.27 million samples from over 17,000 sampling locations (Hartmann, Lauerwald, et al., 2014). The watersheds of the GLORICH database sampling locations were geometrically intersected with the recent loess areal extent and the hydrochemical data extracted and analyzed. For each sampling location the mean and median values were calculated. In the following, all analyses are based on the mean values since the median values are not significantly different (see Supplemental Material B). Additional data on some rivers draining the Chinese Loess Plateau were added by extracting chemical data from literature (Ran et al., 2015, 2017; Ran, Lu, et al., 2017; Xiao et al., 2016; Zhang et al., 2013) and creating watersheds for the sampling points in *ArcMap*. The fractions of loess as well as all other lithologies from the Global Lithological Map Database (GLiM) (Hartmann & Moosdorf, 2012) within the watersheds were calculated. Mean annual runoff and temperature values were extracted for the sampling locations from Fekete et al. (2002) and Hijmans et al. (2005), respectively.

2.5. Global Calculations of Alkalinity Flux Rates and CO_2 Consumption

The calculations of alkalinity fluxes and CO_2 consumption were done twice for each time step (LGM, Mid-Holocene, and recent times), one scenario considering loess deposits and one scenario neglecting loess deposits, using only the lithology from the Global Lithological Map Database (GLiM, Hartmann & Moosdorf, 2012, only considering the first level information "xx" for all polygons and therefore substituting possible loess deposits reported in the GLiM by other or generalized lithologies, because loess is only reported in sublevel information "yy"). The lithological maps were compiled in ArcGIS and merged following a specific order (Figure 2). If loess data were available from the GUM database (attributes: xx = El/Er/Ea), these polygons were merged with the GLiM shapefile, which serves as a background lithological map.

For all lithologies, apart from carbonate sedimentary rocks and loess deposits, an alkalinity flux model was applied, which is based on a spatially explicit runoff-dependent model of chemical weathering, calibrated for 381 catchments in Japan (Hartmann, 2009) and which was later enhanced by considering temperature and a soil-shielding effect (Hartmann, Moosdorf, et al., 2014). The different weathering model equations for each lithological class applied to calculate alkalinity fluxes are described in the supporting information (Supplemental Material C, Table S1) and were first used to quantify global alkalinity fluxes by Goll et al. (2014). These equations distinguish between alkalinity fluxes from carbonate and silicate weathering.

For the carbonate sedimentary rocks, the following carbonate weathering functions were applied and the results compared:

1. Romero-Mujalli, Hartmann, and Börker (2018)

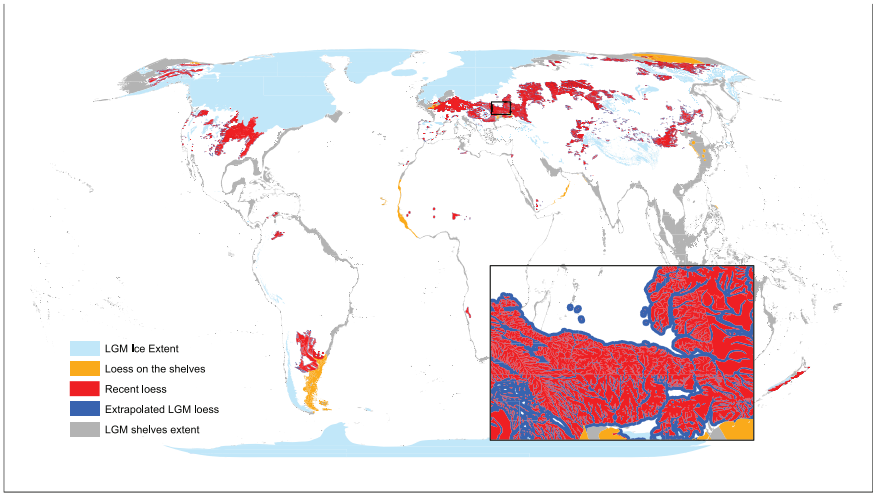

Figure 3. Differences in reconstructed global loess distribution between the LGM and recent times. The recent loess distribution is shown in red, and the extrapolated areas for the LGM are shown in blue. The orange color represents the redrawn loess on the continental shelves, and the gray color represents the general shelves extent that was exposed during LGM. The LGM ice cover is shown in light blue.

$$\log_{10}\text{alk} = \left(e^{b1+b2*T+b3*T^2}\right) \tag{1}$$

with alk = alkalinity in meq L^{-1}, T = mean annual land temperature in °C, $b1 = -1.73$, $b2 = 0.28$, $b3 = -0.0157$, and a standard deviation of the function of 0.2 (logarithm of meq L^{-1}).

The range of uncertainty in the global calculations was calculated using the standard deviation of the function as follows:

$$\text{Uncertainty of the global flux} = \sum(\text{Flux per grid} * 0.2 * \log(10)) \tag{2}$$

2. Amiotte-Suchet and Probst (1995)

$$\text{alk} = 3.1692 * q \tag{3}$$

with alk = alkalinity rate in meq alkalinity m^{-2} a^{-1} and q = runoff in mm^3 mm^{-2} a^{-1}.

3. Bluth and Kump (1994)

$$\text{alk} = \frac{10^{4.521}(0.1 * q)^{0.934}}{1{,}000} \tag{4}$$

with alk = alkalinity rate in meq alkalinity m^{-2} a^{-1} and q = runoff in mm a^{-1}.

The residual standard deviations for the models in this study were calculated after

$$\text{residual standard deviation} = \sqrt{\frac{\sum(\text{residuals})^2}{n-1}} \tag{5}$$

with residuals = observed flux − estimated flux.

The ice sheet extent for the LGM was taken from Ehlers et al. (2011), and the LGM land mask was given by the shelves extent calculated from ETOPO1 (see section 2.2.2). For the Mid-Holocene the same land-sea

Table 1
Differences in Loess Areal Extent, Comparing LGM and Mid-Holocene/Recent Times

	LGM	Mid-Holocene/recent
Loess on continents [$\times 10^6$ km^2]	9.28	4.91
Loess on exposed continental shelves [$\times 10^6$ km^2]	1.85	0
Total loess [$\times 10^6$ km^2]	11.13	4.91

mask as for nowadays was applied (land coverage derived by GLiM coverage, Hartmann & Moosdorf, 2012, and GUM coverage, Börker et al., 2018, respectively). Temperature and runoff data for each time period were taken from Earth System Model outputs of the Max-Planck-Institute (surface runoff and near-surface air temperature for the LGM, Mid-Holocene, and pre-industrial, Jungclaus et al., 2012a, 2012b, 2012c). These data had to be pre-processed by calculating the annual mean values of monthly data. The runoff data for the LGM had to be extrapolated from the continents to the exposed continental shelf areas in ArcMap, because the shelf areas were not fully covered by runoff data due to the raster resolution of the input data set.

The lithological coverage, as well as the ice extent, LGM land mask, carbonate content of the ocean sediments, soil-shielding, temperature, and runoff data were converted to a 20 × 20 km grid to run the global calculations.

3. Results and Discussion

3.1. Changes in Loess Area

While the recent loess coverage is about 5×10^6 km^2, the areal extent during the LGM was ~11×10^6 km^2 in our 10 km extrapolation (Figure 3 and Table 1).

Extrapolating the recent loess area to the LGM is a theoretical approximation, because a constant increase in the areal extent around recent loess deposits is assumed. Kohfeld and Harrison (2001) (DIRTMAP database) report on an expansion of loess deposits downwind of deserts and ice sheets and a general increase of loess mass accumulation rates of 1–5 times during the LGM. The Chinese Loess Plateau was extended to the south of the Yangtze River (25–30°N) (Pinxian & Xiangjun, 1994, and references therein), which is resulting in about a doubling of the extent of the modern Chinese Loess Plateau. In order to get a global doubling of the loess extent for LGM times as first-order approximation, the value of 10 km was chosen for the extrapolation method.

Since there exists no paleogeographic sedimentary pattern for all the continental shelves, which are submerged nowadays, or the continental land area during the LGM, it might also be possible that the LGM loess extent is underestimated or overestimated. Besides, loess, which might be present in alluvial sediments, for example, and which would have an influence on alkalinity fluxes as well, is not considered separately as loess in our calculations for the scenario of recent times.

The classification of carbonate content in marine sediments reveals the following proportions of lithologies on the exposed continental shelves:

1. without loess: 24% siliciclastic sediments, 21% mixed sediments, and 55% carbonate sediments
2. with loess: 20% siliciclastic sediments, 18% mixed sediments, 51% carbonate sediments, and 11% loess sediments

The lithological map of Gibbs and Kump (1994), used in various studies (Ludwig et al., 1999; Munhoven, 2002) to quantify weathering fluxes from the exposed continental shelf areas, provides similar results (55% of siliciclastic sediments and 45% of carbonate sediments as described in Ludwig et al., 1999).

3.2. Chemical Weathering of Loess

Zhang et al. (2013) observe a dominance of loess weathering on the weathering fluxes even at 18% watershed loess coverage. Therefore, here a rounded value of 20% loess coverage as boundary condition to identify catchments with significant loess weathering contribution is used in the following analysis.

Of the geospatial data of the recent loess distribution and the watersheds of the GLORICH sampling points, and the additional data for the Chinese Loess Plateau, 1,032 sampling locations have watersheds that are covered by more than 20% loess; 683 sampling locations feature alkalinity and/or major ion data (Ca^{2+}). The majority of data points are from the United States and China (Figure 4).

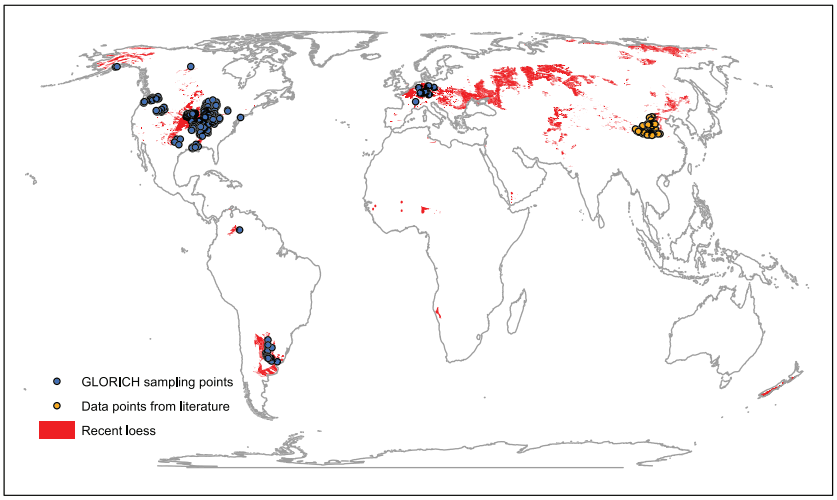

Figure 4. Locations of the water sampling stations, whose watersheds have more than 20% loess coverage and relevant water chemistry data. The GLORICH sampling points are shown in blue, and the additional data points taken from literature are shown in orange. The red areal extent represents the recent loess deposits (Börker et al., 2018).

Mean alkalinity concentrations and standard deviation in samples with a significant loess coverage of >20% is ~4,110 ± 2,400 μeq L^{-1}, whereas the global average river alkalinity concentration and standard deviation is ~1,850 ± 1,920 μeq L^{-1}, suggesting that loess weathering contributes disproportionally to alkalinity in river water and therefore to elevated fluxes compared to the lithological base below the loess deposits.

3.2.1. Regional Observed Differences in Loess Weathering

The different lithologies below the loess (loess fraction >0.2) do not show a significant pattern in their influence on the alkalinity concentration in global river waters (Figure 5a). Therefore, it is assumed that the base lithology below the loess does not affect significantly the study of loess weathering and is neglected, which is also supported by the study of Zhang et al. (2013). However, where carbonate sedimentary rocks underlie loess deposits, this may not be the case, and their possible effect on loess weathering fluxes is additionally considered.

Furthermore, it was tested whether loess sediments show globally homogeneous weathering patterns. Alkalinity in rivers draining catchments with loess (areal loess fraction >0.2) shows a distinct land surface temperature dependency, comparable to carbonate weathering patterns (Romero-Mujalli, Hartmann, & Börker, 2018), with some deviations from the patterns for Argentina (Figures 5a and 5b). The analysis of major ions reveals some regional differences in the composition of the water (Figures 5c–5f), which will be explained below.

The Ca^{2+}/Mg^{2+} concentrations in the river water (Figure 5c), above the dashed line, representing the ratio of $Ca^{2+}/Mg^{2+} = 2$, indicate that carbonate minerals other than calcite (e.g., dolomite) or silicate minerals may be a relevant Ca^{2+} source (Romero-Mujalli, Hartmann, & Börker, 2018). While the loess regions of France, Germany, Venezuela, Canada, and Argentina seem less affected by non-calcite contributions, data from China show the largest positive deviation from the 2:1 ratio. For the United States, Goddéris et al. (2013) report that dolomite weathering occurs in the loess pedons, which might be reflected here. Dolomite occurrences are also reported for the Chinese Loess Plateau (e.g., Meng et al., 2015). The Ca^{2+}/SO_4^{2-} ratio (Figure 5d) shows that most of the water sampling points lay above the 10:1 ratio (mentioned by Romero-Mujalli, Hartmann, & Börker, 2018; Romero-Mujalli, Hartmann, Börker, Gaillardet, et al., 2018; and Gaillardet et al., 2018, as a border for calcite weathering evaluation), which may indicate an influence of sulfate mineral dissolution (Romero-Mujalli, Hartmann, & Börker, 2018) or anthropogenic inputs as pyrite oxidation might be excluded, assuming that particles transported via air are oxidized quickly. Especially Argentinian and Chinese loess deposits show elevated SO_4^{2-} concentrations (ratio of $Ca^{2+}/SO_4^{2-} \sim 1$), which could be related to evaporation processes. In addition, data points with a $Ca^{2+}/Na^{+} < 10$ (Figure 5e) might be influenced by evaporite dissolution or silicate weathering (Gaillardet et al., 1999),

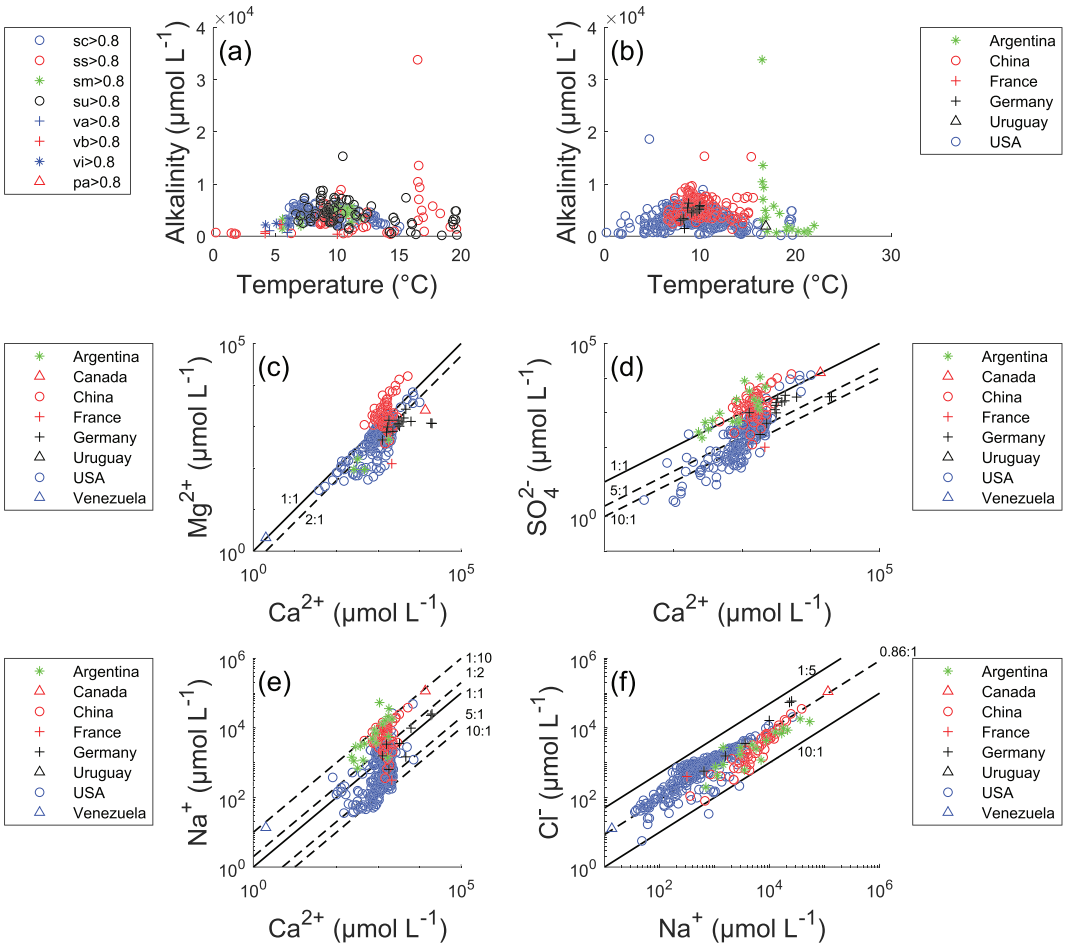

Figure 5. (a) Alkalinity concentration versus temperature for loess deposits with a catchment fraction >0.2, grouped by the underlying bedrock (sc = carbonate sedimentary rocks, ss = siliciclastic sedimentary rocks, sm = mixed sedimentary rocks, su = unconsolidated sediments, va = acid volcanic rocks, vb = basic volcanic rocks, vi = intermediate volcanic rocks, pa = acid plutonic rocks). (b) The dependency of alkalinity concentrations in rivers draining loess (fraction >0.2), grouped after regions, shows that the Argentinian and Chinese loess have in general higher alkalinity concentrations. Major ion concentrations in rivers draining loess deposits (fraction >0.2) with Ca^{2+}/Mg^{2+} (c), Ca^{2+}/SO_4^{2-} (d), Ca^{2+}/Na^{+} (e), and Na^{+}/Cl^{-} (f).

which is the case for almost all samples. Many data points have a ratio different from Na^{+}/Cl^{-} ~ 0.86 (Figure 5f), which indicates that the Na^{+} and Cl^{-} concentrations are affected by other sources than sea salt (ratio molar Na^{+}/Cl^{-} ~ 0.86; Möller, 1990).

The general cation distribution pattern suggests that Ca^{2+} is the primary cation released (Figure 6), supporting that calcite might be the dominant contributor, whereas Na^{+} contributes ~20% to the total cation equivalent concentration. Ternary diagrams of the distribution of major cations in the water samples draining loess deposits (fraction >0.2) can be additionally seen in the supporting information, showing that carbonate sedimentary rocks provide in general lower concentrations of Na^{+} and K^{+} compared to loess deposits.

Since loess mineralogy is dependent on the provenance and the primary lithologies that it is derived from, it is challenging to find the one typical weathering signature for all regions of loess. The Argentinian loess might be influenced by an input of volcanic ash (Zárate, 2003) or evaporitic processes within the river catchments and therefore shows elevated concentrations of Na^{+} or SO_4^{2-}. Evaporation can be expected in some regions of the Chinese Loess Plateau since it is the largest arid and semi-arid zone in China (Huang et al., 2008), which might explain elevated concentrations of SO_4^{2-} or Na^{+}. Moreover, dolomite contribution to alkalinity fluxes, which is represented by elevated Mg^{2+} concentrations, might be expected for regions of

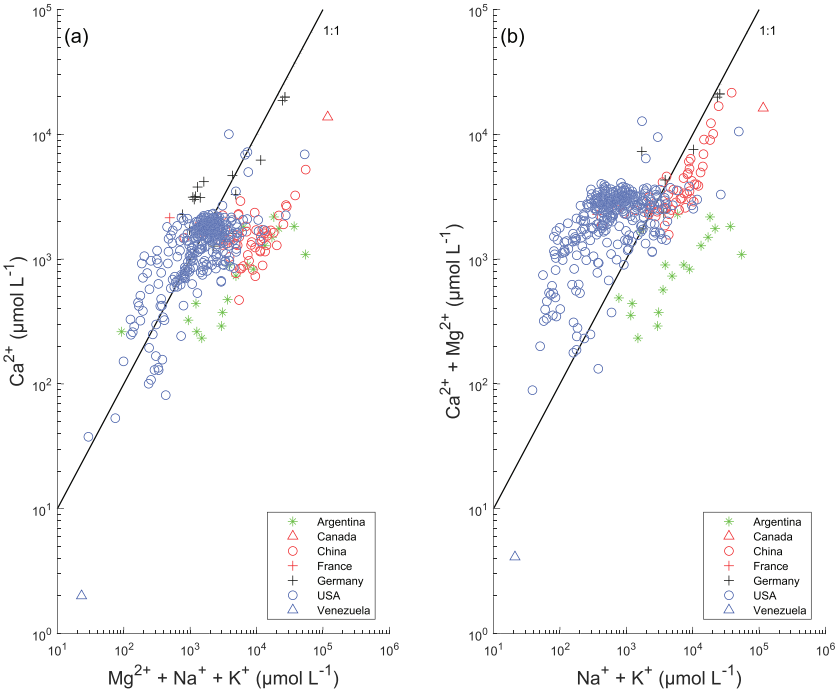

Figure 6. The ratio of Ca^{2+} versus $Mg^{2+} + Na^{+} + K^{+}$ (a) and ratio of $Ca^{2+} + Mg^{2+}$ versus $Na^{+} + K^{+}$ (b) in the water samples draining watersheds of >20% of loess coverage. The solid line represents the 1:1 line. Note that for cations where no data were available the value was set to 0 for comparison.

the Chinese loess deposits and some regions of the loess deposits of the United States (Goddéris et al., 2013; Meng et al., 2015).

3.3. Comparison With Previous Carbonate Weathering Functions

To test the hypothesis that loess weathering derived alkalinity fluxes are comparable to carbonate rock alkalinity fluxes at the broader scale, previous global carbonate weathering models were compared with the new data set compiled here. Used global carbonate weathering functions are runoff dependent (Amiotte-Suchet & Probst, 1995; Bluth & Kump, 1994) and include in case of the function for calcite weathering (Romero-Mujalli, Hartmann, & Börker, 2018) a temperature adjustment, comparable in shape as shown for loess alkalinity in Figures 5a and 5b. The general increase in alkalinity with increasing temperature up to ~11°C in the model of Romero-Mujalli, Hartmann, and Börker (2018) can be explained by increasing biological activity and hence elevated soil-rock pCO_2 driving the weathering reactions. However, for higher temperatures (>11°C) alkalinity concentrations in rivers seem to decrease, which is related to the temperature effect on the carbonate system (Romero-Mujalli, Hartmann, & Börker, 2018). Gaillardet et al. (2018) analyzed the climate control on carbonate weathering using $Ca^{2+} + Mg^{2+}$ concentrations to display the intensity of carbonate weathering and found that the maximum of carbonate weathering intensity can be observed with mean annual air temperatures between 5°C and 15°C following a bell-shaped curve, which is consistent with the results of Romero-Mujalli, Hartmann, and Börker (2018).

These identified bell-shaped patterns for calcite weathering conditions are also observed using all water samples whose catchments have a loess fraction >0.2 and showing alkalinity and $Ca^{2+} + Mg^{2+}$ concentrations dependent on temperature (Figures 7 and 8). Both figures show the identified function of Romero-Mujalli, Hartmann, and Börker (2018) with its range of the calculated uncertainty for comparison.

Despite the above identified bell-shaped pattern, it has to be stressed out that the function of Romero-Mujalli, Hartmann, and Börker (2018) was trained for catchments with predominant calcite weathering, while catchments with significant Mg^{2+} contribution showed a tendency to elevated alkalinity values.

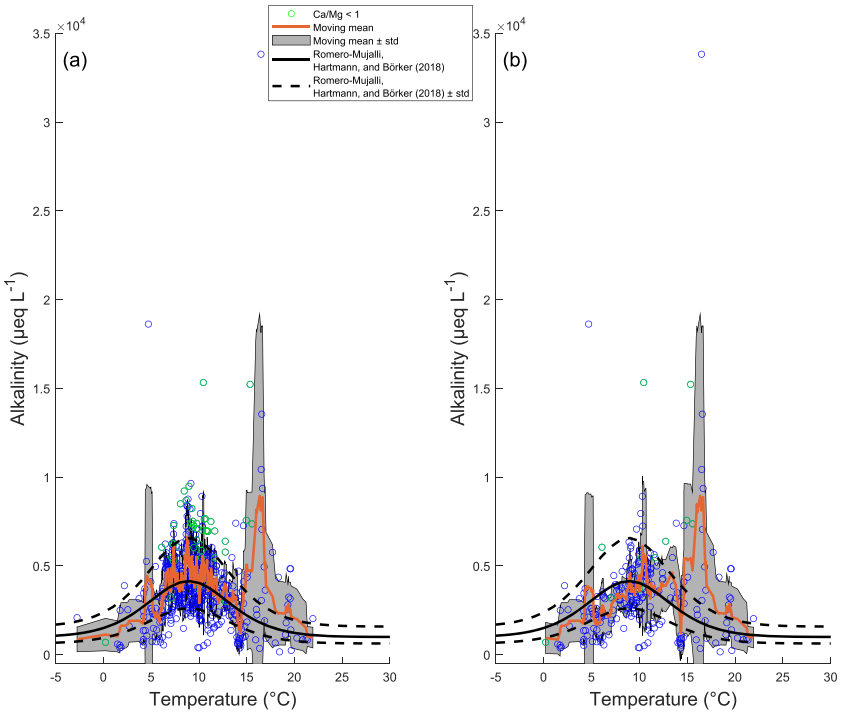

Figure 7. Alkalinity concentration of river catchments with a loess fraction >0.2 correlate with mean annual surface temperature (a). Carbonate sedimentary rocks as underlying lithology were excluded (sc > 0.2) to test their influence on the alkalinity concentrations (b). The solid black line in both plots represents the function for carbonate weathering identified by Romero-Mujalli, Hartmann, and Börker (2018) with the range of uncertainty as dashed lines for typical calcite weathering. The green points indicate water samples with $Ca^{2+}/Mg^{2+} < 1$ and show that outliers are partly because of elevated Mg^{2+} concentrations. In the range around 15°C and 18°C outliers are partly from the Argentinian area with likely elevated silicate contribution (cf. Figure 5b). Additionally, the moving mean value of alkalinity concentration is shown (in orange) with the range of the standard deviation (in gray).

Therefore, this approach is reasonable for weathering from lithologies with dominant calcite weathering but might underestimate alkalinity fluxes for other sources that add, for example, Mg^{2+}. The elevated concentrations in both alkalinity data and $Ca^{2+} + Mg^{2+}$ data (Figures 7 and 8), in comparison to the idealized calcite weathering function, might be due to the dissolution of further carbonate minerals (e.g., dolomite, indicated by elevated Mg^{2+} concentrations), silicate minerals, or catchment internal processes like evaporation. However, low runoff areas have a tendency to elevated concentrations (Figure 9). For temperatures between 15°C and 20°C some data points show clearly elevated alkalinity values in comparison to the model of Romero-Mujalli, Hartmann, and Börker (2018) and are mostly data from Argentina, which might be dominated by silicate weathering due to an input of volcanic ash and predominantly volcanic rocks as source rock (Zárate, 2003). Nevertheless, the bias in the global calculations might be small considering that regions with mean annual temperatures between 15°C and 20°C cover nowadays only ~13% and for the LGM ~20% of the ice- and water-free land area (temperature data set used for the pre-industrial and LGM in this study, resolution 20 × 20 km, land mask derived by the consideration of all lithologies used for calculations in this study), and this tendency is mostly restricted to the Argentinean area.

While the alkalinity concentration patterns seem to show a bell-shaped pattern, dependent on temperature, runoff is in general the dominant control on the flux, which is intended to be modeled in the following. Alkalinity concentrations of river waters draining loess sediments (fraction >0.2) generally decrease with increasing runoff (Figure 10a). The dilution effect seems to be strong after a threshold of about 200 mm a^{-1} (Figures 10a and 10b), and ~26% of all recent global loess deposit areas have runoff values >200 mm a^{-1}, indicating that a dilution effect should be considered in global calculations of loess weathering.

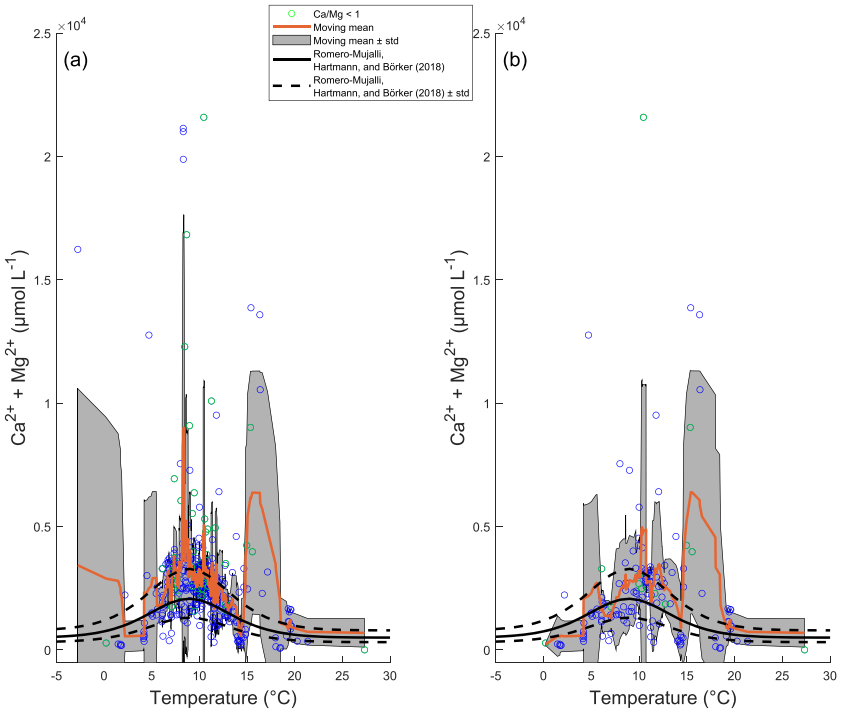

Figure 8. $Ca^{2+} + Mg^{2+}$ concentration of river catchments with a loess fraction >0.2, dependent on mean annual surface temperature (a). Carbonate sedimentary rocks as underlying lithology were excluded (sc > 0.2) to test their influence on the water chemical species (b). The solid black line represents in both plots the function for carbonate weathering identified by Romero-Mujalli, Hartmann, and Börker (2018) with the range of uncertainty as dashed lines for typical calcite weathering. The green points indicate water samples with $Ca^{2+}/Mg^{2+} < 1$. Additionally, the moving mean value of the $Ca^{2+} + Mg^{2+}$ concentration is shown (in orange) with the range of the standard deviation (in gray).

Therefore, a new alkalinity flux function was developed, based on a nonlinear regression method for observed alkalinity flux rates (Figure 10b) applying a four-parameter logistic function, which fits best the observed data points and allows to project alkalinity flux rates for high runoff areas. One parameter was set manually to 9 to represent the maximum values of alkalinity flux rate in the observations:

$$\log_{10}\text{alkalinity flux rate} = \frac{9}{1+\exp^{-a(\log_{10}\text{runoff}+b)}} + c,\ \text{MSE} = 0.08 \quad (6)$$

with $\log_{10}$alkalinity flux rate in µeq km^{-2} a^{-1}, $\log_{10}$runoff in mm^3 mm^{-2} a^{-1}, $a = 0.63$, $b = 0.76$, and $c = -2.00$.

The range of uncertainty in the global calculations of Equation 6 was calculated as follows:

$$\text{Uncertainty of the global flux} = \sum(\text{Flux per grid*0.08*log(10)}) \quad (7)$$

The uncertainties of the alkalinity flux rates for the four models (observed-estimated, Equation 5) show the smallest residual standard deviation for the model of Romero-Mujalli, Hartmann, and Börker (2018) (0.5×10^6 µeq m^{-2} a^{-1}), whereas for Amiotte-Suchet and Probst (1995), Bluth and Kump (1994), and the new function the values are 1×10^6, 4.2×10^6, and 2.7×10^6 µeq m^{-2} a^{-1}, respectively.

The residual analysis of the modeled alkalinity flux rates for the four carbonate weathering models compared to different variables (Figure 11) shows in general no clear trend with temperature, but a tendency toward overestimation with elevated runoff (Figures 11b, 11f, 11j, and 11n). The relative residual distribution is additionally shown in the supporting information.

The new loess function (Equation 6) provides the best estimation for the observed alkalinity flux rates with an $R^2 = 0.46$ ($R^2 = 0.42$ for Romero-Mujalli, Hartmann, & Börker, 2018; $R^2 = 0.33$ for Amiotte-Suchet &

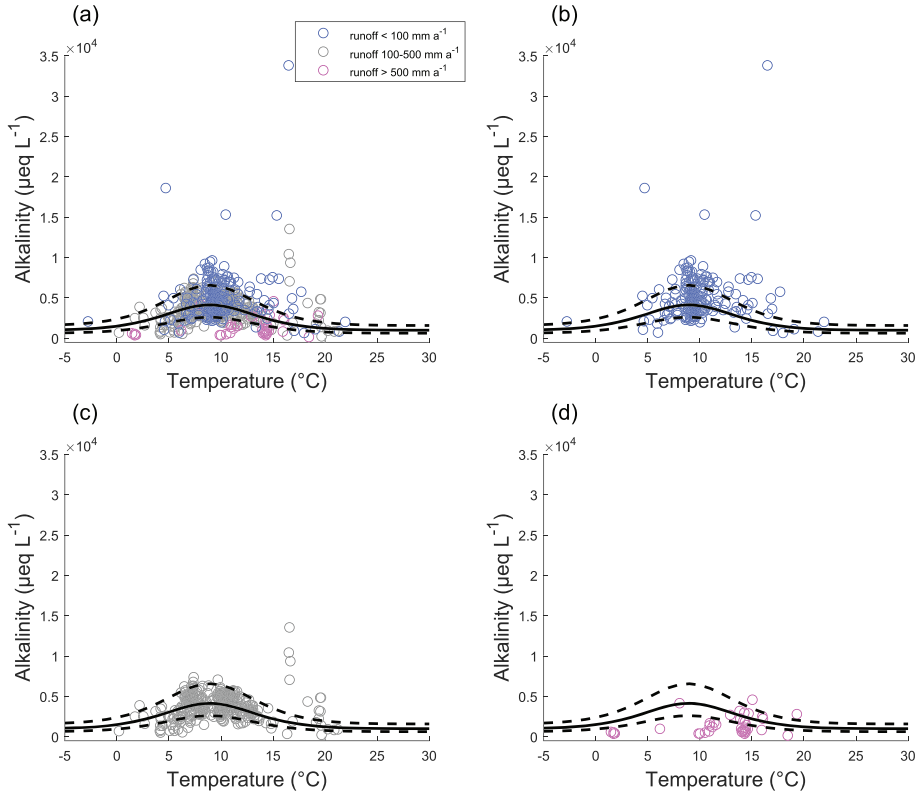

Figure 9. Alkalinity concentration of river catchments with a loess fraction >0.2, dependent on temperature and grouped after runoff, for all classes of runoff (a), for runoff <100 mm a^{-1} (b), for runoff between 100 and 500 mm a^{-1} (c), and for runoff >500 mm a^{-1} (d). The solid black line represents the function for carbonate weathering identified by Romero-Mujalli, Hartmann, and Börker (2018) with the range of the uncertainty as dashed lines for typical calcite weathering.

Probst, 1995; and $R^2 = 0.34$ for Bluth & Kump, 1994). The model of Romero-Mujalli, Hartmann, and Börker (2018), however, shows a reduced dispersion for temperature (excluding extreme values), while for the runoff-dependent models the residuals show a higher dispersion and seem to display the "bell-shaped pattern" (Figures 11e, 11i, and 11m). They might underestimate alkalinity flux rates for temperatures about 10°C, but for lower and higher temperatures, the runoff-dependent models might overestimate alkalinity fluxes. Moreover, it can be seen that all previous models for carbonate weathering overestimate fluxes for high runoff values significantly at the $p < 0.05$ level (Figures 11b, 11f, and 11j), whereas the new loess function (Equation 6) considering the dilution effect is not ($p = 0.25$). Still, for high runoff values the loess function overestimates alkalinity fluxes. But this bias might be relatively small considering that alkalinity fluxes from elevated runoff regions (>200 mm a^{-1}) contribute with ~30% to total alkalinity fluxes from loess deposits, while their areal extent is about 26% of the global loess area. Nevertheless, although the new loess function overestimates alkalinity flux rates for high runoff values (Figure 11n), most of the alkalinity flux rates (~80% of the loess grids in the global calculation for the recent setting) are underestimated. This might be related to the residuals of the new function comparing for alkalinity concentration in the rivers (Figure 11p).

Although the model of Romero-Mujalli, Hartmann, and Börker (2018) considers as well the climate variable temperature, it might underestimate global alkalinity fluxes from loess deposits because the inputs of, for instance, Mg-minerals like dolomite are neglected. The carbonate weathering functions of Amiotte-Suchet and Probst (1995) and Bluth and Kump (1994) represent total carbonate weathering fluxes, including other carbonate minerals than calcite. Nevertheless, they assume almost constant alkalinity values (the dilution effect in the equation of Bluth & Kump, 1994, is relatively weak), which is not consistent with the observed alkalinity concentrations in rivers draining loess deposits (Figure 12). For the global alkalinity

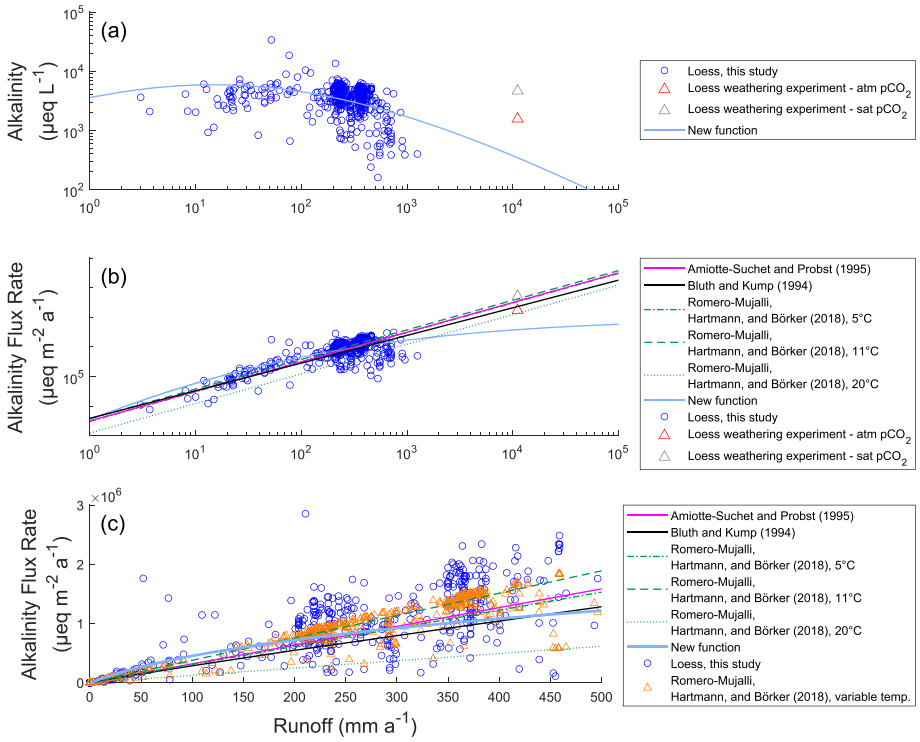

Figure 10. Relationship between runoff and loess-derived alkalinity concentration (a) and relationship between runoff and loess-derived alkalinity flux rate (b) with the previous models of Amiotte-Suchet and Probst (1995), Bluth and Kump (1994), and Romero-Mujalli, Hartmann, and Börker (2018) and the new function for comparison. The red triangle represents the sample of a loess column experiment under atmospheric pCO_2 conditions (mean alkalinity concentration ~1,600 μeq L^{-1}), and the gray triangle the loess column experiment under saturated pCO_2 conditions (mean alkalinity concentration ~4,700 μeq L^{-1}), preventing the dilution effect by forcing percolation of all water (cf. Supplemental Material D). The relationship between the loess-derived alkalinity flux rate and runoff for different models is shown in (c), for runoff values between 0 and 500 mm a^{-1}. The orange triangles show here the dispersion of alkalinity flux rate values considering the surface temperature of the sampling locations applying the temperature-depending model of Romero-Mujalli, Hartmann, and Börker (2018).

flux calculations the new function for loess weathering (Equation 6) was applied since it can better estimate alkalinity fluxes from loess deposits and considers better the dilution effect for regions with high runoff values.

3.4. Global Alkalinity Fluxes Including Loess Deposits

For the global calculations of alkalinity flux and CO_2 consumption rates from loess deposits the new function (Equation 6), whereas for carbonate sedimentary rocks the models of Romero-Mujalli, Hartmann, and Börker (2018), Amiotte-Suchet and Probst (1995), and Bluth and Kump (1994) were used, and their results are listed in Tables 2 and 3 and Figure 13. For simplicity, in the following, the global alkalinity flux and CO_2 consumption values are compared for the different time slices applying the model of Romero-Mujalli, Hartmann, and Börker (2018) for carbonate sedimentary rocks. For all other lithologies the model of Goll et al. (2014) was applied. For comparison, the calculations were done for two scenarios: one scenario where loess lithologies are considered for weathering and one where they are neglected. Note that the CO_2 consumption rates of loess deposits might be regarded as the lower boundary, because additional silicate weathering happening in the loess sediments can increase the CO_2 consumption rates.

It can be shown that loess weathering increases the global alkalinity fluxes compared to the base lithology below (~36% for the LGM, ~15% for the Mid-Holocene, and ~16% for recent times). This increase in alkalinity fluxes because of loess weathering might partly explain the gap between the proportion of carbonate

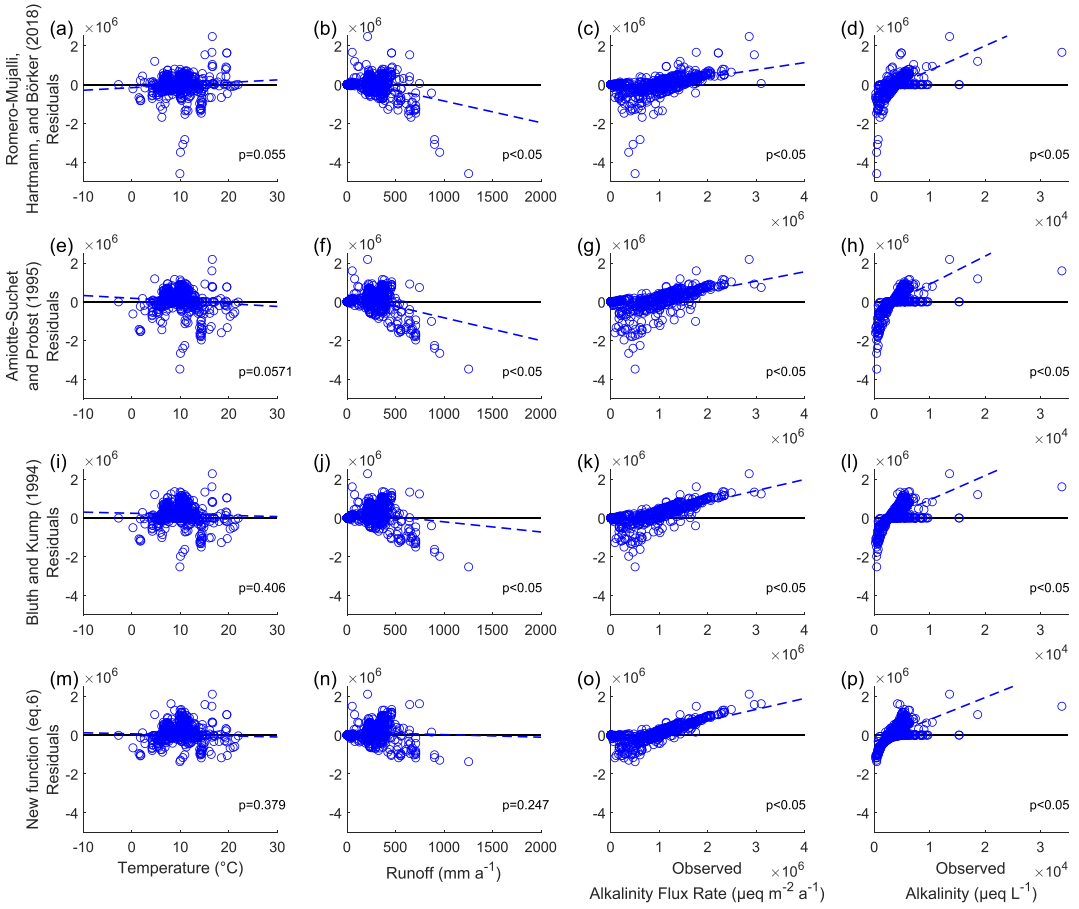

Figure 11. Residual analyses (observed flux-estimated flux) compared to different variables of the four models for Romero-Mujalli, Hartmann, and Börker (2018) (a–d), Amiotte-Suchet and Probst (1995) (e–h), Bluth and Kump (1994) (i–l), and the new function (Equation 6) (m–p). Trendlines are shown in dashed blue. Note that although the new loess function overestimates alkalinity flux rates for high runoff values (n) most of the alkalinity flux rates (~80% of the loess grids in the global calculation for the recent setting) are underestimated. This might be related to the residuals of the new function comparing for alkalinity concentration in the rivers (p).

weathering on global CO_2 consumption fluxes reported by Gaillardet et al. (1999) and those calculated by Hartmann (2009).

The calculated global weathering fluxes are generally lower than estimates from previous studies, which can be explained by in general lower runoff values in the data sets used for the global calculations in this study (Jungclaus et al., 2012a, 2012b, 2012c) to allow a comparison with runoff as a forcing parameter based on the same model outputs. Applying a runoff data set, which was used to calibrate the new loess function (Equation 6) and which includes observed river discharge information (Fekete et al., 2002) for the recent time, yields 106% to 124% higher values (Table 4). Therefore, only the relative changes between time slices are interpreted here.

The differences in alkalinity flux rates between the Mid-Holocene and the present day are generally low (Figure 13); only for loess deposits the alkalinity flux rates during the Mid-Holocene decrease by ~9%. Alkalinity flux rates from silicate weathering are decreasing during the LGM (~30% for the scenario neglecting loess weathering and ~28% for the scenario considering loess weathering if compared to recent times). Moreover, the alkalinity fluxes derived by the carbonate weathering proportion of the model of Goll et al. (2014), which was applied for other lithologies than carbonate sedimentary rocks (sc) and loess, are decreasing during the LGM as well (~25% for the scenario neglecting loess weathering and ~26% for the scenario considering loess weathering).

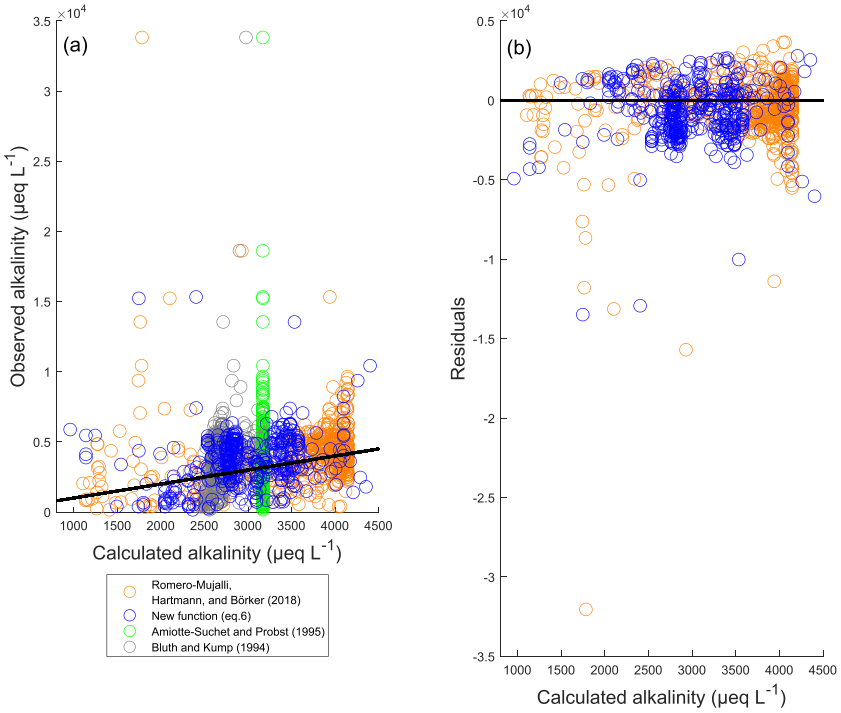

Figure 12. Observed alkalinity concentration in rivers draining loess deposits (loess fraction >0.2) versus calculated alkalinity concentration applying different models. The solid line represents the 1:1 line (a). Residuals distribution applying the model of Romero-Mujalli, Hartmann, and Börker (2018) and the new loess function (Equation 6) (b).

The global alkalinity flux rates from carbonate sedimentary rocks (sc) for the different applied models are regarded separately in the following. Generally, the alkalinity fluxes from carbonate sedimentary rocks are higher for all three models for the LGM compared to the recent time (Figure 13). The values derived by applying the carbonate weathering functions of Amiotte-Suchet and Probst (1995) and Bluth and Kump (1994) show the higher positive deviations (mean of both models: ~55% increase for the scenario considering loess weathering and ~60% increase for the scenario neglecting loess weathering) than the model of Romero-Mujalli, Hartmann, and Börker (2018) (~34% increase considering loess weathering and ~31% increase neglecting loess weathering).

These differences might be explained by the alkalinity flux rates derived from carbonate sedimentary rocks (sc) on the exposed continental shelf areas. Previous studies on changes of weathering fluxes at glacial-interglacial time scales report an increase of global fluxes of about 20% for the LGM time, mostly because of the abundance of carbonate sedimentary rocks on the continental shelves (Gibbs & Kump, 1994; Ludwig et al., 1999). Here, the carbonates of the continental shelf areas contribute to global alkalinity fluxes by about 21% (considering loess weathering, mean of the two runoff-dependent models). This contribution from carbonate sedimentary rocks (sc) on the continental shelves to global alkalinity flux rates is less if applying the model of Romero-Mujalli, Hartmann, and Börker (2018) (~11% considering loess weathering). These differences might be related to an overestimation of the fluxes of the runoff-dependent models for the carbonate sedimentary rocks (sc), mostly located in high temperature regions, on the exposed continental shelf areas because the models do not consider temperature. Runoff as possible reason can be excluded because all three models show a comparable bias for runoff in the residuals (Figures 11b, 11f, 11j, and 11n).

Nevertheless, there remains uncertainty due to the classification of the sediments on the exposed continental shelves. The equations that were used to consider the carbonate content of the shelf sediments were calibrated for consolidated sedimentary rocks (sc), which might not reflect properly the alkalinity flux rates from the continental shelves. However, loess deposits on the continental shelves do not contribute significantly to global alkalinity flux rates (~2% applying the mean of the three models).

Table 2
Contribution of Loess Weathering to Global CO_2 Consumption Rates for Different Time Slices, Compared With Global Weathering Scenarios Neglecting Loess Weathering

		LGM [Mt C a^{-1}]		Mid-Holocene [Mt C a^{-1}]		Recent [Mt C a^{-1}]	
Model		With loess	Without loess	With loess	Without loess	With loess	Without loess
Silicate-dominated lithologies (su, vb, pb, py, va, vi, partly: mt, ss, pi, sm, pa)[a]	Goll et al. (2014)	28 + 3[b]	28 + 3[b]	44	45	43	44
Carbonate-influenced lithologies (partly: mt, ss, pi, sm, pa)[a]	Goll et al. (2014)	12 + 2[b]	13 + 2[b]	20	20	20	20
Carbonate sedimentary rocks (sc)	Romero-Mujalli, Hartmann, and Börker (2018)	12 [6;17] + 8 [4;12][b]	13 [7;18] + 9 [5;13][b]	15 [8;22]	16 [8;23]	15 [8;21]	16 [9;23]
Carbonate sedimentary rocks (sc)	Amiotte-Suchet and Probst (1995)	17 + 18[b]	18 + 19[b]	23	23	22	24
Carbonate sedimentary rocks (sc)	Bluth and Kump (1994)	14 + 16[b]	16 + 16[b]	19	20	19	20
Loess	(Equation 6)	18 [15;22] + 2 [2;3][b]	—	11 [9;13]	—	12 [10;14]	—
Total, with sc from Romero-Mujalli, Hartmann, and Börker (2018)		85 ± 8	68 ± 7	90 ± 8	81 ± 8	90 ± 7	80 ± 7
Total, with sc from Amiotte-Suchet and Probst (1995)		100	83	98	88	97	88
Total, with sc from Bluth and Kump (1994)		95	78	94	85	94	84

Note. For Romero-Mujalli, Hartmann, and Börker (2018) and the new function the range of uncertainty of the global calculations is given in the brackets. The combination of both uncertainty estimations was derived as follows: total uncertainty $= \sqrt{(\text{uncertainty Romero} - \text{Mujalli et al.}(2018)^2 + \text{uncertainty new function}^2)}$.
[a]su = unconsolidated sediments, sm = mixed sedimentary rocks, ss = siliciclastic sedimentary rocks, va = acid volcanic rocks, vb = basic volcanic rocks, vi = intermediate volcanic rocks, pa = acid plutonic rocks, pb = basic plutonic rocks, pi = intermediate plutonic rocks, py = pyroclastics, mt = metamorphics. [b]Values that are calculated for the exposed continental shelves.

The elevated alkalinity fluxes during the LGM from loess sediments including those from shelves (approximately +78% compared to recent times) might be slightly too high because the loess regions during the LGM show colder temperatures (with a mean of about −3°C), which might lead to an overestimation of fluxes for the runoff-dependent new function (Equation 6). Applying the temperature- and runoff-dependent model of Romero-Mujalli, Hartmann, and Börker (2018) for the loess deposits shows an increase of about 20% of loess-derived alkalinity fluxes compared to recent times. Nevertheless, there exists a lack of data points for low temperature regions, but because the residuals of the new loess function (Equation 6) show a smaller range for the parameter temperature than the other models, it might be reasonable to apply the new loess function for loess weathering (Equation 6) as first-order approximation.

With the new loess weathering function and applying the model of Romero-Mujalli, Hartmann, and Börker (2018) for carbonate sedimentary rocks (sc) to avoid an overestimation of alkalinity fluxes from the exposed continental shelves during the LGM, the differences in the total global alkalinity fluxes between the LGM and recent times become small (~4% increase for the LGM). Without the consideration of loess weathering the differences in alkalinity fluxes between the LGM and recent times become larger (~11% decrease during the LGM). However, the estimated extent of the continental loess area represents conservative assumptions, discussed in the next section.

3.4.1. Sensitivity of Loess-Derived Alkalinity Fluxes to Their Areal Extent

Increased alkalinity fluxes due to loess deposits are especially interesting because mapped loess deposits (excluding the shelves) nowadays cover only about 4% of the global ice-free land area (relative to the GLiM area without ice and water bodies; Hartmann & Moosdorf, 2012). Still, the influence on global alkalinity fluxes and CO_2 consumption rates could become even larger because the loess areal extent reported

Table 3
Contribution of Loess Weathering to Global Alkalinity Flux Rates for Different Time Slices, Compared With Global Weathering Scenarios Neglecting Loess Weathering

		LGM [Mt C a^{-1}]		Mid-Holocene [Mt C a^{-1}]		Recent [Mt C a^{-1}]	
	Model	With loess	Without loess	With loess	Without loess	With loess	Without loess
Silicate-dominated lithologies (su, vb, pb, py, va, vi, partly: mt, ss, pi, sm, pa)[a]	Goll et al. (2014)	28 + 3[b]	28 + 3[b]	44	45	43	44
Carbonate-influenced lithologies (partly: mt, ss, pi, sm, pa)[a]	Goll et al. (2014)	25 + 4[b]	26 + 4[b]	40	41	39	40
Carbonate sedimentary rocks (sc)	Romero-Mujalli, Hartmann, and Börker (2018)	23 [13;34] + 16 [9;24][b]	25 [14;37] + 17 [9;25][b]	30 [16;43]	31 [17;46]	29 [16;43]	32 [17;46]
Carbonate sedimentary rocks (sc)	Amiotte-Suchet and Probst (1995)	33 + 37[b]	37 + 38[b]	45	47	45	47
Carbonate sedimentary rocks (sc)	Bluth and Kump (1994)	28 + 31[b]	31 + 33[b]	38	39	38	40
Loess	(Equation 6)	37 [30;44] + 4 [4;5][b]	—	21 [17;25]	—	23 [19;28]	—
Total, with sc from Romero-Mujalli, Hartmann, and Börker (2018)		140 ± 15	103 ± 14	135 ± 14	117 ± 15	134 ± 14	116 ± 15
Total, with sc from Amiotte-Suchet and Probst (1995)		171	136	150	133	150	131
Total, with sc from Bluth and Kump (1994)		160	125	143	125	143	124

Note. For Romero-Mujalli, Hartmann, and Börker (2018) and the new function the range of uncertainty of the global calculations is given in the brackets. The combination of both uncertainty estimations was derived as follows: total uncertainty $= \sqrt{(\text{uncertainty Romero} - \text{Mujalli et al.}(2018)^2 + \text{uncertainty new function}^2)}$.
[a] su = unconsolidated sediments, sm = mixed sedimentary rocks, ss = siliciclastic sedimentary rocks, va = acid volcanic rocks, vb = basic volcanic rocks, vi = intermediate volcanic rocks, pa = acid plutonic rocks, pb = basic plutonic rocks, pi = intermediate plutonic rocks, py = pyroclastics, mt = metamorphics. [b] Values that are calculated for the exposed continental shelves.

in the Global Unconsolidated Sediments Map (GUM) (Börker et al., 2018) underestimates the land area where loess weathering occurs due to neglected thin loess covers that were not mapped in the input geological maps. Some literature studies report a recent global loess cover of even about 10% (Muhs & Bettis, 2003; Pécsi, 1990). Nevertheless, these maps are of a coarser resolution.

Taking the LGM loess cover derived by the 10 km extrapolation method (without loess on the shelves) and applying it for the recent climate setting results in a mean increase of about 34% for alkalinity flux rates and about 25% for CO_2 consumption rates if compared to the recent alkalinity flux and CO_2 consumption rates without loess. Because the extrapolated LGM loess cover partly includes river valleys and therefore alluvial sediments, which might contain relevant amounts of loess nowadays, the approach of comparing global alkalinity fluxes derived by loess deposits might be seen as conservative, since the distributed LGM loess might still influence recent weathering fluxes. This aspect should be further studied, to quantify the legacy contribution of old loess deposits to differently mapped lithological units in recent global maps.

Further, to test the influence of the extrapolated LGM loess area on the global alkalinity fluxes, a sensitivity experiment was conducted. The extrapolation method was, additionally to 10 km, also done with 5 and 20 km. Besides, the alkalinity fluxes for the LGM were calculated assuming the same loess distribution than for recent times (in the following named "0 km"). A possible upper boundary of loess weathering might be given by applying modeled dust output data. Kohfeld and Harrison (2001) report eolian mass accumulation rates (MARs) for loess deposits during the LGM of 50 to more than 1,000 g m^{-2} a^{-1}. Taking the dust model output data for the LGM from Albani et al. (2016) and applying a lower boundary of 50 g m^{-2} a^{-1} as a specific minimum of total dust deposition in order to form a loess deposit show elevated loess alkalinity flux rates (in

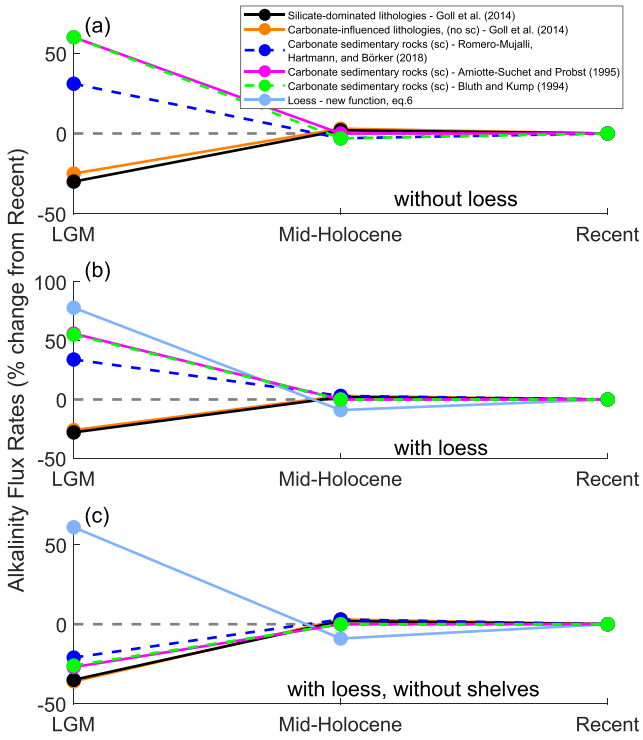

Figure 13. Comparison of the alkalinity flux rates of the different time slices, without the consideration of loess deposits (a) and with loess deposits (b). Panel (c) shows the changes in alkalinity flux rates, without the continental shelves. Note that the two dashed lines showing the alkalinity flux rate calculations for the models of Amiotte-Suchet and Probst (1995) (in pink) and of Bluth and Kump (1994) (in green) for carbonate sedimentary rocks (sc) overlap. Additionally, note that the equations used to calculate alkalinity fluxes for all other lithologies apart from carbonate sedimentary rocks (sc) and loess from Goll et al. (2014) distinguish between alkalinity fluxes derived by carbonate weathering and by silicate weathering (explanation in the supporting information).

the following simulations named after the method "50MAR"). But results from this method might be too high because the dust MARs include as well smaller particles than those typical for loess deposits. Nevertheless, taking the output data of the same model (Albani et al., 2016) for the pre-industrial time, it can be seen that the areal extent for dust deposits with a deposition rate of more than 50 g m^{-2} a^{-1} is about half as large as the extent during the LGM. This observation underlines the reasonability of the 10 km loess extrapolation method. The differences between the scenarios are shown in Table 5 and Figure 14.

The sensitivity of the global alkalinity flux rates to the loess areal extent scenarios becomes evident when comparing the differences between global alkalinity fluxes of the LGM and recent times (Figure 14d). While the application of the possible lower boundary (0 km) of loess areal extent suggests almost no changes between the global alkalinity fluxes as if compared to neglecting loess deposits, the increase of the loess areal

Table 4
Global Alkalinity Flux Rates and CO_2 Consumption Rates for the Recent Time Applying the Runoff Data Set of Fekete et al. (2002) and Applying the LGM Loess Cover (Without Shelves)

	Recent-MPI runoff [Mt C a^{-1}]	Recent-Fekete et al. (2002) runoff [Mt C a^{-1}]	Change to recent MPI runoff [%]	Recent-applying LGM loess cover + MPI runoff [Mt C a^{-1}]	Change to recent MPI runoff [%]
Alkalinity flux rates	134 ± 14	276 ± 27	+106	156 ± 15	+16
CO_2 consumption rates	90 ± 7	202 ± 14	+124	100 ± 8	+11

Table 5
Differences in Total Global Alkalinity Flux Rates for the LGM Applying Several Loess Area Extrapolation Scenarios

Extrapolation scenario	Loess area [10^6 km^2]	Proportion on global LGM area [%]	LGM alkalinity flux rates from loess deposits [Mt C a^{-1}]	Global total alkalinity flux rates at the LGM considering three different models for carbonate sedimentary rocks (sc) and including loess alkalinity flux rates [Mt C a^{-1}]; with their relative change to the global alkalinity flux rates for the recent time, including loess weathering		
				Romero-Mujalli, Hartmann, and Börker (2018)	Amiotte-Suchet and Probst (1995)	Bluth and Kump (1994)
0 km	6.40	4.86	22	122; −9%	153; +2%	143; 0%
5 km	9.40	7.14	34	133; −1%	164; +9%	154; +8%
10 km	11.13	8.46	41	140; +4%	171; +14%	160; +12%
20 km	13.81	10.49	52	149; +11%	179; +19%	169; +18%
50MAR	26.66	20.26	73	163; +22%	192; +28%	182; +27%

Note. For all calculations in this study a modeled runoff data set was used, in which runoff is generally underestimated and hence generally lower weathering flux values are produced as if compared to values reported in previous studies. Therefore, the key information from the table is the relative change between the scenarios, which are shown in Figure 14d.

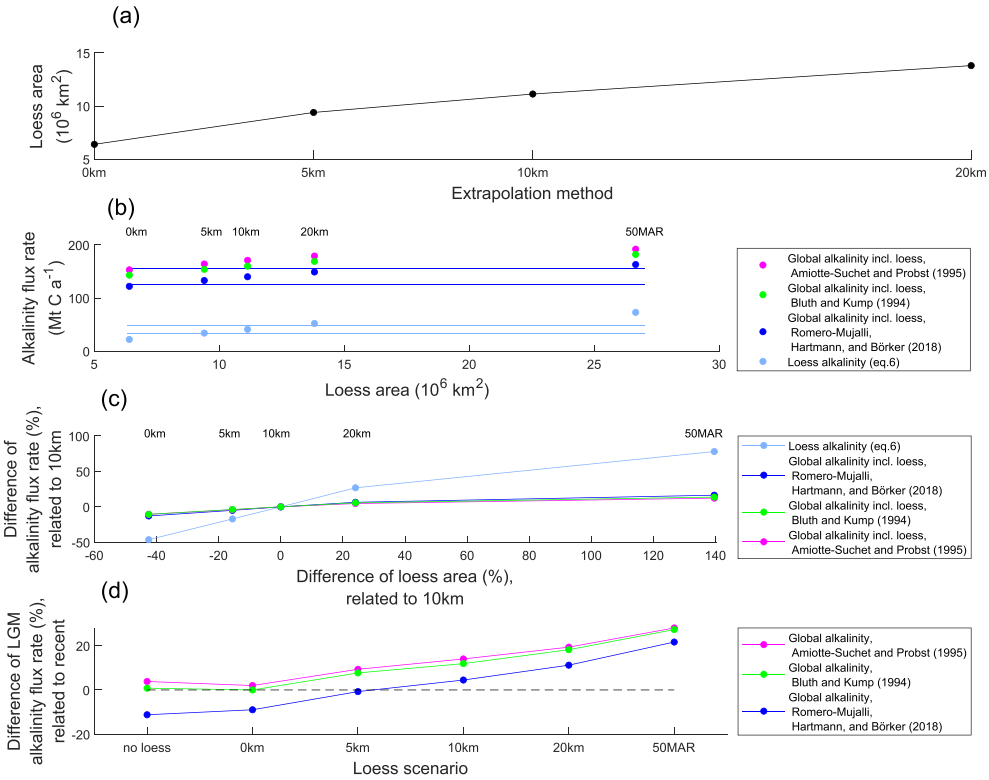

Figure 14. Sensitivity of loess areal extent on alkalinity flux rates during the LGM. Panel (a) shows the changes in loess area due to different distances applied in the extrapolation. Panel (b) distinguishes loess alkalinity flux rates and global alkalinity flux rates, applying different models, for five different scenarios for the LGM time slice. The solid lines show the uncertainties for global alkalinity flux rates and loess alkalinity flux rates applying the 10 km extrapolation method. Panel (c) shows the relative changes in loess areal extent and alkalinity flux rates related to the 10 km extrapolation method used in this study. (d) Changes of global alkalinity flux differences between recent times and the LGM considering different loess scenarios. Note that for the loess scenario "no loess" the LGM alkalinity fluxes are related to the recent fluxes without the consideration of loess, whereas for all other LGM loess scenarios are related to the recent alkalinity fluxes considering loess weathering.

extent during the LGM (scenario 10 km to 50MAR), increases the global alkalinity flux rates up to 22–28% during the LGM compared to recent times.

4. Conclusion

Loess sediments are widespread around the globe nowadays. Although they can be very heterogeneous regarding their mineralogy, depending on their provenance or internal processes like evaporation, they show, in general, a similar weathering behavior than carbonate sedimentary rocks. Studying the chemical composition of river water draining loess areas shows elevated alkalinity fluxes if compared to idealized calcite weathering and points to the importance of recognizing further minerals and their weathering behavior into more detailed global loess weathering models like dolomite, silicates, or sulfate minerals because they would affect alkalinity concentrations. Furthermore, it can be noticed that more data on cold temperature regions, especially interesting for the LGM, are needed to improve the quantification of loess weathering fluxes. Based on the river chemical data used in this study, a new empirical function for loess weathering was developed, which considers a dilution effect for elevated runoff areas.

Applying the new loess weathering function in global calculations suggests that loess contributes significantly to global alkalinity flux rates, with about 16%. But it remains to be tested if the global alkalinity fluxes from loess deposits are possibly underestimated, because small and/or thin loess covers might not be mapped as loess but still influence the water chemistry. Gaillardet et al. (1999) report on a larger proportion of carbonate weathering on global CO_2 consumption fluxes than calculated by Hartmann et al. (2009) taking a different approach. This gap could be partly explained by loess weathering.

Comparing the LGM and recent times shows very similar global alkalinity flux rates (~4% higher alkalinity flux rates during the LGM for one of the discussed scenarios). The suggested enhanced fluxes from loess sediments during the LGM are hereby counteracting the modeled and in general lower silicate weathering rates during the LGM. Thus, loess sediments might be involved in stabilizing the alkalinity fluxes at glacial-interglacial time scales, which points to the importance of further consideration of sediments, and specifically their origin, in global weathering models.

Data Availability Statement

Data for this research are archived in the PANGAEA database (https://doi.org/10.1594/PANGAEA.915793).

Acknowledgments
Funding for this work has been provided by German Research Foundation (DFG) through the Cluster of Excellence CLISAP2 (DFG Exec177, Universität Hamburg) and BMBF-project PALMOD (Ref 01LP1506C) through the German Federal Ministry of Education and Research (BMBF) as Research for Sustainability initiative (FONA). The authors thank the editor, Christian Zeeden, and one anonymous reviewer for constructive comments on the manuscript.

References

Albani, S., Mahowald, N. M., Murphy, L. N., Raiswell, R., Moore, J. K., Anderson, R. F., et al. (2016). Paleodust variability since the Last Glacial Maximum and implications for iron inputs to the ocean. *Geophysical Research Letters*, *43*, 3944–3954. https://doi.org/10.1002/2016GL067911

Amante, C., & Eakins, B., (2009). ETOPO1 1 arc-minute global relief model: Procedures, data sources and analysis. National Geophysical Data Center, NOAA, Boulder Colorado.

Amiotte-Suchet, P., & Probst, J. L. (1995). A global model for present-day atmospheric/soil CO2 consumption by chemical erosion of continental rocks (GEM-CO2). *Tellus B*, *47*(1–2), 273–280.

Biryukov, V. Y., Faustova, M. A., Kaplin, P. A., Pavlidis, Y. A., Romanova, E. A., & Velichko, A. A. (1988). The paleogeography of Arctic shelf and coastal zone of Eurasia at the time of the last glaciation (18,000 yr BP). *Palaeogeography, Palaeoclimatology, Palaeoecology*, *68*(2–4), 117–125. https://doi.org/10.1016/0031-0182(88)90034-X

Bluth, G. J., & Kump, L. R. (1994). Lithologic and climatologic controls of river chemistry. *Geochimica et Cosmochimica Acta*, *58*(10), 2341–2359.

Börker, J., Hartmann, J., Amann, T., & Romero-Mujalli, G. (2018). Terrestrial sediments of the Earth: Development of a Global Unconsolidated Sediments Map database (GUM). *Geochemistry, Geophysics, Geosystems*, *19*, 997–1024. https://doi.org/10.1002/2017GC007273

Bostock, H., Jenkins, C., Mackay, K., Carter, L., Nodder, S., Orpin, A., et al. (2018). Distribution of surficial sediments in the ocean around New Zealand/Aotearoa. Part B: Continental shelf. *New Zealand Journal of Geology and Geophysics*, 1–22.

Buggle, B., Glaser, B., Hambach, U., Gerasimenko, N., & Marković, S. (2011). An evaluation of geochemical weathering indices in loess–paleosol studies. *Quaternary International*, *240*(1–2), 12–21.

Dürr, H. H., Meybeck, M., & Dürr, S. H. (2005). Lithologic composition of the Earth's continental surfaces derived from a new digital map emphasizing riverine material transfer. *Global Biogeochemical Cycles*, *19*, GB4S10. https://doi.org/10.1029/2005GB002515

Ehlers, J., Gibbard, P. L., & Hughes, P. D. (2011). *Quaternary glaciations—Extent and chronology: A closer look* (Vol. 15). Amsterdam: Elsevier.

Fekete, B. M., Vörösmarty, C. J., & Grabs, W. (2002). High-resolution fields of global runoff combining observed river discharge and simulated water balances. *Global Biogeochemical Cycles*, *16*(3), 1042. https://doi.org/10.1029/1999GB001254

Gaillardet, J., Calmels, D., Romero-Mujalli, G., Zakharova, E., & Hartmann, J. (2018). Global climate control on carbonate weathering intensity. *Chemical Geology*, 118762. https://doi.org/10.1016/j.chemgeo.2018.05.009

Gaillardet, J., Dupré, B., Louvat, P., & Allègre, C. J. (1999). Global silicate weathering and CO2 consumption rates deduced from the chemistry of large rivers. *Chemical Geology*, *159*(1–4), 3–30.
Gibbs, M. T., & Kump, L. R. (1994). Global chemical erosion during the last glacial maximum and the present: Sensitivity to changes in lithology and hydrology. *Paleoceanography and Paleoclimatology*, *9*(4), 529–543.
Goddéris, Y., Brantley, S. L., François, L. M., Schott, J., Pollard, D., Déqué, M., & Dury, M. (2013). Rates of consumption of atmospheric CO2 through the weathering of loess during the next 100 yr of climate change. *Biogeosciences*, *10*(1), 135–148. https://doi.org/10.5194/bg-10-135-2013
Goff, J. A., Jenkins, C. J., & Williams, S. J. (2008). Seabed mapping and characterization of sediment variability using the usSEABED data base. *Continental Shelf Research*, *28*(4–5), 614–633.
Goll, D. S., Moosdorf, N., Hartmann, J., & Brovkin, V. (2014). Climate-driven changes in chemical weathering and associated phosphorus release since 1850: Implications for the land carbon balance. *Geophysical Research Letters*, *41*, 3553–3558. https://doi.org/10.1002/2014GL059471
Hartmann, J. (2009). Bicarbonate-fluxes and CO2-consumption by chemical weathering on the Japanese Archipelago—Application of a multi-lithological model framework. *Chemical Geology*, *265*(3–4), 237–271.
Hartmann, J., Jansen, N., Dürr, H. H., Kempe, S., & Köhler, P. (2009). Global CO2-consumption by chemical weathering: What is the contribution of highly active weathering regions? *Global and Planetary Change*, *69*(4), 185–194.
Hartmann, J., Lauerwald, R., & Moosdorf, N. (2014). A brief overview of the GLObal RIver CHemistry Database, GLORICH. *Procedia Earth and Planetary Science*, *10*, 23–27.
Hartmann, J., Lauerwald, R., & Moosdorf, N. (2019). GLORICH—Global river chemistry database, supplement to: Hartmann, J et al. (2014): A brief overview of the GLObal RIver Chemistry Database, GLORICH. *Procedia Earth and Planetary Science*, *10*, 23–27. https://doi.org/10.1016/j.proeps.2014.08.005
Hartmann, J., & Moosdorf, N. (2012). The new global lithological map database GLiM: A representation of rock properties at the Earth surface. *Geochemistry, Geophysics, Geosystems*, *13*, Q12004. https://doi.org/10.1029/2012GC004370
Hartmann, J., Moosdorf, N., Lauerwald, R., Hinderer, M., & West, A. J. (2014). Global chemical weathering and associated P-release—The role of lithology, temperature and soil properties. *Chemical Geology*, *363*, 145–163.
Hijmans, R. J., Cameron, S. E., Parra, J. L., Jones, P. G., & Jarvis, A. (2005). Very high resolution interpolated climate surfaces for global land areas. *International Journal of Climatology*, *25*(15), 1965–1978.
Huang, J., Zhang, W., Zuo, J., Bi, J., Shi, J., Wang, X., et al. (2008). An overview of the semi-arid climate and environment research observatory over the Loess Plateau. *Advances in Atmospheric Sciences*, *25*(6), 906–921. https://doi.org/10.1007/s00376-008-0906-7
Jenkins, C. (1997). Building offshore soils databases. *Sea Technology*, *38*, 25–28.
Jenkins, C.J., (2018). dbSEABED: Information integration system for marine substrates. Univ. Colorado, Boulder, USA. http://tinyurl.com/dbseabed/dbseabed.htm, .
Jungclaus, J., Giorgetta, M., Reick, C., Legutke, S., Brovkin, V., Crueger, T., et al. (2012a). CMIP5 simulations of the Max Planck Institute for Meteorology (MPI-M) based on the MPI-ESM-P model: The lgm experiment, served by ESGF.
Jungclaus, J. Giorgetta, M., Reick, C., Legutke, S., Brovkin, V., Crueger, T., et al. (2012b). CMIP5 simulations of the Max Planck Institute for Meteorology (MPI-M) based on the MPI-ESM-P model: The midHolocene experiment, served by ESGF
Jungclaus, J., Giorgetta, M., Reick, C., Legutke, S., Brovkin, V., Crueger, T., et al. (2012c). CMIP5 simulations of the Max Planck Institute for Meteorology (MPI-M) based on the MPI-ESM-P model: The piControl experiment, served by ESGF.
Kohfeld, K. E., & Harrison, S. P. (2001). DIRTMAP: The geological record of dust. *Earth-Science Reviews*, *54*(1–3), 81–114.
Kump, L., & Alley, R. B. (1994). Global chemical weathering on glacial time scales. In *Material fluxes on the surface of the Earth* (pp. 46–60). Washington, DC: National Academy Press.
Lambeck, K., Rouby, H., Purcell, A., Sun, Y., & Sambridge, M. (2014). Sea level and global ice volumes from the Last Glacial Maximum to the Holocene. *Proceedings of the National Academy of Sciences*, *111*(43), 15,296–15,303.
Lefort, J.-P., Danukalova, G., & Monnier, J.-L. (2013). Why the submerged sealed beaches, last remnants of the low stands of the Upper Pleistocene regression, are better expressed in the Western than in the Eastern English Channel? *Geo-Eco-Marina*, *19*, 5.
Li, T., Wang, C., & Li, P. (2013). Loess deposit and loess landslides on the Chinese Loess Plateau. In F. Wang, M. Miyajima, T. Li, W. Shan, & T. F. Fathani (Eds.), *Progress of geo-disaster mitigation technology in Asia*, (pp. 235–261). Berlin Heidelberg, Berlin, Heidelberg: Springer.
Ludwig, W., Amiotte-Suchet, P., & Probst, J.-L. (1999). Enhanced chemical weathering of rocks during the last glacial maximum: A sink for atmospheric CO2? *Chemical Geology*, *159*(1), 147–161.
Mahowald, N., Kohfeld, K., Hansson, M., Balkanski, Y., Harrison, S. P., Prentice, I. C., et al. (1999). Dust sources and deposition during the last glacial maximum and current climate: A comparison of model results with paleodata from ice cores and marine sediments. *Journal of Geophysical Research*, *104*(D13), 15,895–15,916. https://doi.org/10.1029/1999JD900084
Meng, X., Liu, L., Balsam, W., Li, S., He, T., Chen, J., & Ji, J. (2015). Dolomite abundance in Chinese loess deposits: A new proxy of monsoon precipitation intensity. *Geophysical Research Letters*, *42*, 10,391–10,398. https://doi.org/10.1002/2015GL066681
Möller, D. (1990). The Na/Cl ratio in rainwater and the seasalt chloride cycle. *Tellus B*, *42*(3), 254–262.
Muhs, D. R., & Bettis, E. (2003). Quaternary loess-paleosol sequences as examples of climate-driven sedimentary extremes. *Special Papers-Geological Society of America*, 53–74.
Muhs, D. R., & Bettis, E. A. (2000). Geochemical variations in Peoria Loess of western Iowa indicate paleowinds of midcontinental North America during last glaciation. *Quaternary Research*, *53*(1), 49–61.
Muhs, D. R., Cattle, S. R., Crouvi, O., Rousseau, D. D., Sun, J. M., & Zarate, M. A. (2014). In P. Knippertz, & J. W. Stuut (Eds.), *Loess records, mineral dust*, (pp. 411–441). Verlag: Springer.
Munhoven, G. (2002). Glacial–interglacial changes of continental weathering: Estimates of the related CO2 and $HCO3^{-}$ flux variations and their uncertainties. *Global and Planetary Change*, *33*(1–2), 155–176.
Pécsi, M. (1990). Loess is not just the accumulation of dust. *Quaternary International*, *7*, 1–21.
Pinxian, W., & Xiangjun, S. (1994). Last glacial maximum in China: Comparison between land and sea. *Catena*, *23*(3–4), 341–353.
Purdy, E.G., (1974). Reef configurations: Cause and effect.
Pye, K. (1984). Loess. *Progress in Physical Geography*, *8*(2), 176–217.
Ran, L., Li, L., Tian, M., Yang, X., Yu, R., Zhao, J., et al. (2017). Riverine CO2 emissions in the Wuding River catchment on the Loess Plateau: Environmental controls and dam impoundment impact. *Journal of Geophysical Research: Biogeosciences*, *122*, 1439–1455. https://doi.org/10.1002/2016JG003713
Ran, L., Lu, X. X., & Liu, S. (2017). Dynamics of riverine CO2 in the Yangtze River fluvial network and their implications for carbon evasion. *Biogeosciences*, *14*(8), 2183–2198.

Ran, L., Lu, X. X., Richey, J. E., Sun, H., Han, J., Yu, R., et al. (2015). Long-term spatial and temporal variation of CO_2 partial pressure in the Yellow River, China. *Biogeosciences*, *12*(4), 921–932. https://doi.org/10.5194/bg-12-921-2015

Romero-Mujalli, G., Hartmann, J., & Börker, J. (2018). Temperature and CO2 dependency of global carbonate weathering fluxes—Implications for future carbonate weathering research. *Chemical Geology*.

Romero-Mujalli, G., Hartmann, J., Börker, J., Gaillardet, J., & Calmels, D. (2018). Ecosystem controlled soil-rock pCO2 and carbonate weathering—Constraints by temperature and soil water content. *Chemical Geology*.

Rousseau, D. D., Chauvel, C., Sima, A., Hatté, C., Lagroix, F., Antoine, P., et al. (2014). European glacial dust deposits: Geochemical constraints on atmospheric dust cycle modeling. *Geophysical Research Letters*, *41*, 7666–7674. https://doi.org/10.1002/2014GL061382

Ryan, W. B. F., Pitman III, W. C., Major, C. O., Shimkus, K., Moscalenko, V., Jones, G. A., et al. (1997). An abrupt drowning of the Black Sea shelf at 7.5 kyr BP. *Geo-Eco-Marina*, *2*, 115–125.

Schaetzl, R. J., Bettis, E. A. III, Crouvi, O., Fitzsimmons, K. E., Grimley, D. A., Hambach, U., et al. (2018). Approaches and challenges to the study of loess—Introduction to the LoessFest Special Issue. *Quaternary Research*, *89*(3), 563–618. https://doi.org/10.1017/qua.2018.15

Smalley, I., Marković, S. B., & Svirčev, Z. (2011). Loess is [almost totally formed by] the accumulation of dust. *Quaternary International*, *240*(1–2), 4–11.

United States Army Corps of Engineers, (1974). Illinois Waterway duplicate locks: Environmental impact statement.

Violante, R. A., Paterlini, C. M., Marcolini, S. I., Costa, I. P., Cavallotto, J. L., Laprida, C., et al. (2014). Chapter 6 The Argentine continental shelf: Morphology, sediments, processes and evolution since the Last Glacial Maximum. *Geological Society, London, Memoirs*, *41*(1), 55–68. https://doi.org/10.1144/M41.6

Xiao, J., Zhang, F., & Jin, Z. (2016). Spatial characteristics and controlling factors of chemical weathering of loess in the dry season in the middle Loess Plateau, China. *Hydrological Processes*, *30*(25), 4855–4869.

Zárate, M. (2003). Loess of southern South America. *Quaternary Science Reviews*, *22*(18–19), 1987–2006.

Zhang, F., Jin, Z., Li, F., Yu, J., You, C. F., & Zhou, L. (2013). The dominance of loess weathering on water and sediment chemistry within the Daihai Lake catchment, northeastern Chinese Loess Plateau. *Applied Geochemistry*, *35*, 51–63. https://doi.org/10.1016/j.apgeochem.2013.05.013